



Fusion Landsat-8 Thermal TIRS and OLI Datasets for Superior Monitoring and Change Detection using Remote Sensing

Hayder Dibs ¹, Alaa Hussein Ali ² , Nadhir Al-Ansari ^{3*} , Salwan Ali Abed ⁴ 

¹ Water Resources Management Engineering Department, Faculty of Engineering, Al-Qasim Green University, Babylon, Iraq.

² Building and Construction Techniques Engineering Department, Al-Mustaqbal University College, 51001 Hillah, Babylon, Iraq.

³ Department of Civil Environmental and Natural Resources Engineering, Lulea University of Technology, 97187 Lulea, Sweden.

⁴ College of Science, University of Al-Qadisiyah, Diwaniyah, 58001, Iraq.

Abstract

Currently, updating the change detection (CD) of land use/land cover (LU/LC) geospatial information with high accuracy outcomes is important and very confusing with the different classification methods, datasets, satellite images, and ancillary dataset types available. However, using just the low spatial resolution visible bands of the remotely sensed images will not provide good information with high accuracy. Remotely sensed thermal data contains very valuable information to monitor and investigate the CD of the LU/LC. So, it needs to involve the thermal datasets for better outcomes. Fusion plays a big role to map the CD. Therefore, this study aims to find out a refining method for estimating the accurate CD method of the LU/LC patterns by investigating the integration of the effectiveness of the thermal satellite data with visible datasets by (a) adopting a noise removal model, (b) satellite images resampling, (c) image fusion, combining and integrating between the visible and thermal images using the Grim Schmidt spectral (GS) method, (d) applying image classification using Mahalanobis distances (MH), Maximum likelihood (ML) and artificial neural network (ANN) classifiers on datasets captured from the Landsat-8 TIRS and OLI satellite system, these images were captured from operational land imager (OLI) and the thermal infrared (TIRS) sensors of 2015 and 2020 to generate about of twelve LC maps. (e) The comparison was made among all the twelve classifiers' results. The results reveal that adopting the ANN technique on the integrated images of the combined TIRS and OLI datasets has the highest accuracy compared to the rest of the applied image classification approaches. The obtained overall accuracy was 96.31% and 98.40%, and the kappa coefficients were (0.94) and (0.97) for the years 2015 and 2020, respectively. However, the ML classifier obtains better results compared to the MH approach. The image fusion and integration of the thermal images improve the accuracy results by 5%–6% from the proposed method better than using low spatial-resolution visible datasets alone.

Keywords:

Thermal TIRS Images;
Change Detection;
Imagery Classification;
Maximum Likelihood Classifier;
Land Cover;
Image Fusion.

Article History:

Received:	12	July	2022
Revised:	22	November	2022
Accepted:	11	December	2022
Available online:	14	February	2023

1- Introduction

The CD plays a big role for the analysts and researchers in different levels of temporal land use and land cover of remote sensing applications such as environment monitoring, disaster assessment, forest management, and urban area expansion [1, 2]. Nowadays, updating the CD of the LU/LC geospatial information with high accuracy outcomes is

* CONTACT: nadhir.alansari@ltu.se

DOI: <http://dx.doi.org/10.28991/ESJ-2023-07-02-09>

© 2023 by the authors. Licensee ESJ, Italy. This is an open access article under the terms and conditions of the Creative Commons Attribution (CC-BY) license (<https://creativecommons.org/licenses/by/4.0/>).

important and very confusing with the variety of classification methods, datasets, satellite images, and ancillary datasets. However, using only the low-spatial-resolution visible bands of the remotely sensed images and conventional techniques will not provide good information with high accuracy [3-5]. On the other side, remotely sensed thermal data contains very valuable information to monitor and investigate the CD of the LU/LC. So, it needs to involve the thermal datasets for better outcomes. In addition, fusion plays a big role in mapping the CD. There are many studies analyzing and processing the CD, as reported by Dibs et al. [6], Dibs et al. [7], and Ramos-Bernal et al. [8]. Currently, the use of the CD is widespread with the increasing numbers of remote sensing satellite systems and sensors that can provide different levels, resolutions, and types of datasets. Add to that the increasing demand for using such analyses as the CD, and the challenges, difficulties, and requirements also will increase with the increasing demands [9-11]. Several studies applied and adopted different models, algorithms, and approaches to the CD [12–15].

A pixel-based CD was known as one of the most popular CD methods [16]. It was widely employed on different satellite images and datasets using different spatial, temporal, and spectral resolutions; random field, conditional random field, and other approaches [11, 15, 17]. The Object-Oriented Based algorithm, Object Correlation Coefficient, Object-Oriented Chi-Square, and other CD techniques are widely applied in the detection of the LU/LC patterns [18–20]. Kwarteng & Chavez (1998) studied the CD of LU/LC in Kuwait using multi-temporal Landsat satellite images [21]. Hashim et al. (2021) studied the detection of the urbanization development area [22]. Also, other previous works study and investigate the CD of LU/LC around the world [23–25]. It is not so clear, which image classification classifier and procedure to analyze for the investigation of the effectiveness of using and integrating the thermal datasets with the visible images (multi-spectral datasets) to obtain highly accurate results of the CD of LU/LC.

This study aims to find out a refinement procedure for estimating the accuracy of the CD method of the LU/LC patterns by investigating the integration of the effectiveness of the thermal satellite data with visible datasets by the image fusion method (the Grim Schmidt spectral) and then classifying them by different pixel-based image classification approaches. In this study, the Landsat-8 TIRS and OLI images were used to examine the CD in LU/LC to find the best and most accurate procedure. The article is organized to start with a description of the materials and methods to show the proposed methodology and adopted datasets, then the section indicating the experimental aspects of combining the Landsat images of both the TIRS and OLI data, the collecting of training and testing samples, image classification processing, the results, and validation of the obtained results.

2- Materials and Methods

For this study, two Landsat-8 images were adopted and obtained by the OLI and TIRS sensors of the Landsat-8 system to be tested and to show the effectiveness of adopting and using the thermal images to enhance and improve the change patterns in LC. There are many phases to performing this research: (a) the pre-processing stage to remove errors and noise; (b) the processing step is determining the study area; (c) satellite image resampling; (d) thermal and visible image combination; (e) fieldwork to collect the ground control points; and (f) the training and testing samples selecting. However, for the post-processing step (g), different methods of supervised classification, such as ANN, MH, and ML approaches, were adopted on the processed datasets to create twelve maps of the LC. Then, (h) validate all the adopted classifier techniques by applying the confusion matrix approach. Finally, make a statistical comparison between all of the results of each image classification method for all the twelve LC maps obtained from (g). The flowchart of the adopted methodology is depicted in Figure 1.

2-1- Study Area Description

The study area for this study was Baghdad, Iraq. Baghdad city is very famous around the world; it is also the capital of the Republic of Iraq. It locates between the coordinates 33° 11' 38" N to 33° 31' 28" N and 44° 14' 24" E to 44° 35' 26" E. Baghdad city has an area of (2,260.2) km², which is around 5% of the total Iraqi area. Its location is in the alluvial plain, which gave it a desert, Figure 2 describes the study area location. Baghdad city is located among five neighbouring states in the middle of Iraq. It has a population of about 7.5 million people. The mainland of Baghdad city is covered by water bodies, residential areas, vegetation areas, and soil areas. The Baghdad city elevation ranges from 31 to 39 m above the mean sea level. The Baghdad temperature reaches a maximum value of 55 °C as a mean monthly during the summer season and a minimum of 0 °C in the winter season. However, Baghdad's annual rainfall ranges from 50 to 200 mm [26–28].

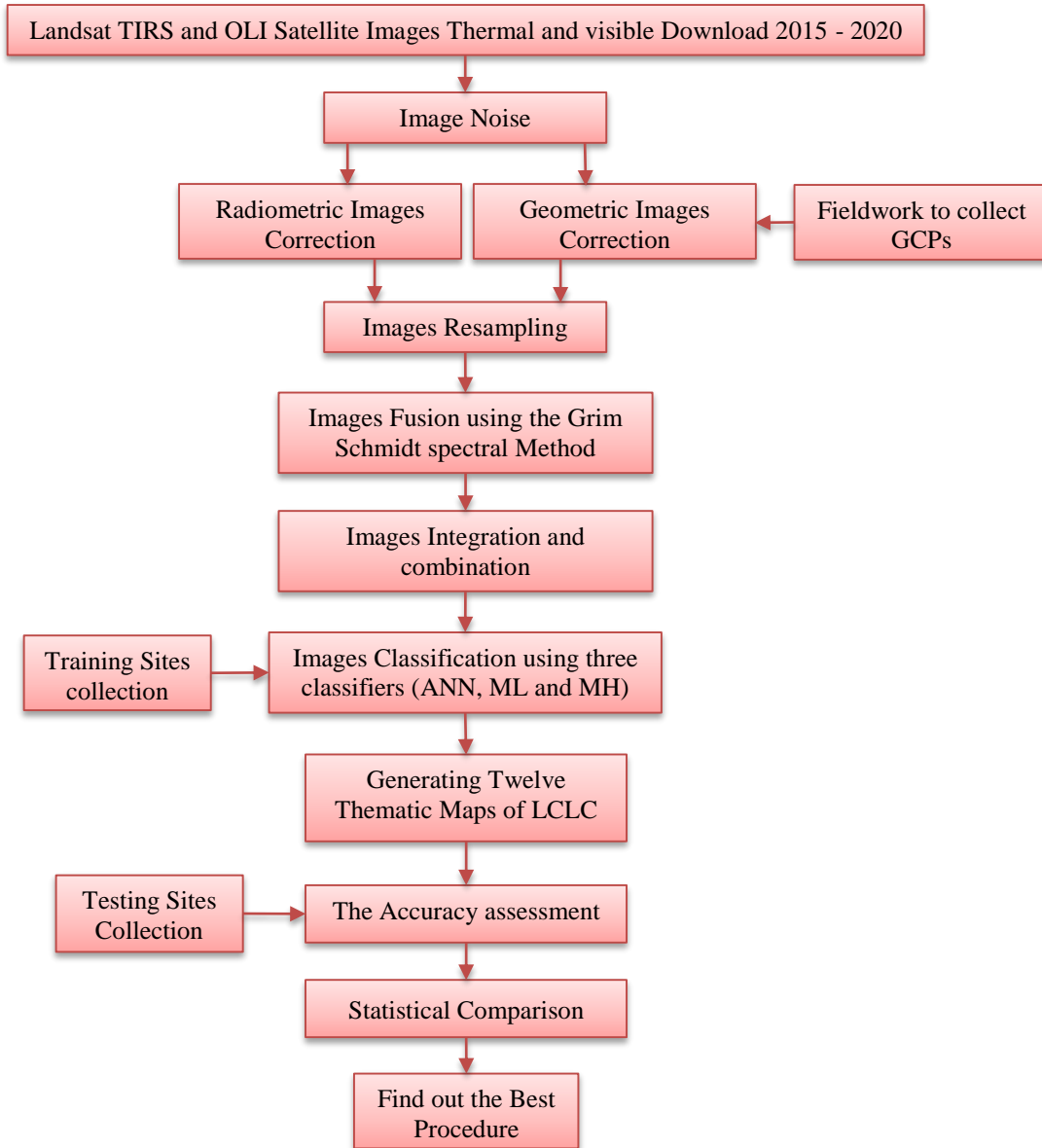


Figure 1. Flowchart of the adopted methodology

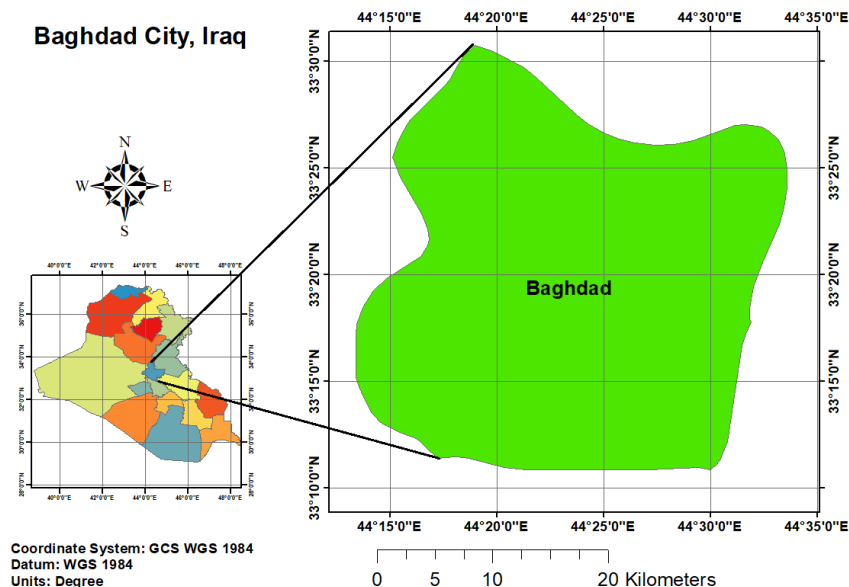


Figure 2. Description of the study area location

2-2- The Satellite Images

The adopted dataset for this research is obtained from the Landsat-8 satellite system. On February 11, 2013, the Landsat-8 satellite was launched into space. The Landsat-8 carries two sensors: the first one is the OLI, and the second one is the TIRS sensor. For this study, visible images were obtained from the Landsat-OLI sensor. However, the thermal datasets were captured from the Landsat-TIRS sensor. The Landsat-8 system has about 11 spectral bands with a spatial resolution of about 30 m for all the bands (1 – 7, 9). However, Band (8) is the panchromatic band; it has a high spatial resolution of about 15 m. Furthermore, the Landsat thermal bands (10 and 11), these bands have a Low-Spatial Resolution of about 100 m. The adopted images for applying to this study were free of charge, and they were downloaded from the website of the U.S. Geological Survey (USGS) (<http://earthexplorer.usgs.gov>). The adopted images have Path = 169 and Row = 37, and both of them are free of clouds. Four Landsat-8 satellite images were used in this study to detect LU/LC change detection; the first two were captured from the OLI Sensor on 12/1/2015 and 26/1/2020, respectively. Another two thermal images were obtained from the Landsat-8 TIRS-sensor on 12/1/2015 and 26/1/2020. Table 1 indicates the specifications of the used images.

Table 1. The specifications of the Landsat-8 of OLI and TIRS datasets

No.	Sensors	Path	Raw	The Applied Dataset bands	Obtained time	Spatial resolution
1	Landsat-OLI	169	37	Red, Green, Blue	12/1/2015	30 m
2	Landsat-OLI	169	37	Red, Green, Blue	26/1/2020	30 m
3	Landsat-TIRS	169	37	Thermal-band 11	12/1/2015	100 m
4	Landsat-TIRS	169	37	Thermal-band 11	26/1/2020	100 m

2-3- Errors Removing and Resampling

Before performing any further analysis on the remote sensing datasets, geometric errors must be removed [29]. In addition, using a good selection of ground truth reference (GTR) locations must be performed. In this study, the geometric correction of all the adopted Landsat-8 images (thermal and visible) was conducted using about 25 GTRs that were collected during the fieldwork in a period between January 12-19, 2020, using the GPS navigator device type Handheld-Garmin GPSMAP-78S. In this research, the reason behind selecting the Handheld-Garmin GPSMAP-78S was because the used satellite images that were selected have a spatial resolution of about 30m and it is very lower compared to the used GPS device accuracy, which means it does not need to use GPS has a higher-accuracy to determining the GTRs locations like a differential GPS device. So, the accuracy of the GPS-78S will be quite enough for using and adopting the Landsat satellite images in this study. The collected GTRs were regularly distributed and located throughout the study area. Table 2 indicates the collected GTRs from the fieldwork. The image geometric correction model was performed by conducting a match between GTRs coordinates to the corresponding points-locations on the used images. The Root-Mean-Square-Error (RMSE) was calculated to identify the accuracy of the applied geometric correction model on the used and adopted satellite images. The RMSE ranged from 0.16 to 0.24.

Table 2. Collected Fieldwork GRTs

No.	Latitude (N)	Longitude (E)	No.	Latitude (N)	Longitude (E)
1	33°30'40.47"	44°20'34.47"	14	33°18'54.67"	44°14'03.64"
2	33°27'53.45"	44°24'32.14"	15	33°22'27.87"	44°17'48.10"
3	33°25'37.98"	44°27'29.91"	16	33°25'36.05"	44°17'05.16"
4	33°23'41.10"	44°27'50.50"	17	33°28'11.37"	44°18'22.57"
5	33°27'08.30"	44°31'53.70"	18	33°25'41.77"	44°20'37.60"
6	33°27'40.41"	44°34'20.46"	19	33°22'04.40"	44°24'21.38"
7	33°26'03.86"	44°34'35.52"	20	33°18'41.75"	44°28'17.49"
8	33°21'57.31"	44°33'26.85"	21	33°16'27.45"	44°26'24.29"
9	33°17'46.30"	44°31'47.87"	22	33°16'58.65"	44°21'52.69"
10	33°11'54.30"	44°29'41.74"	23	33°19'29.27"	44°18'55.50"
11	33°12'02.50"	44°23'32.68"	24	33°14'39.13"	44°19'59.48"
12	33°12'39.15"	44°18'37.18"	25	33°19'32.99"	44°23'58.55"
13	33°16'00.69"	44°15'29.40"			

The first-order polynomial transformation and nearest-neighbour were applied to perform the image geometric corrections and calculate the RMSE. The used projection was the UTM, zone 38N, with WGS-84 as a datum for all of the Landsat-8 images (2015 and 2020). However, image radiometric correction may not be required in this case, only

applying single imagery for conducting imagery classification. In addition, it needs to apply the radiometric correction when using imagery from more than one from the same or different sensor, captured at different times [30]. Currently, researchers and analysts investigate and examine different techniques and methodologies to get the most suitable and accurate results [31]. So, in the coming stage, the radiometric correction will be performed on all four Landsat-8 satellite images (thermal and visible). The radiometric correction is an essential step in performing the image pre-processing to reduce the effects of the sun illumination [32]. The dark object subtraction algorithm was adopted to overcome the radiometric errors of the used Landsat-8 images in this study. In the image processing stages, the processing of the image sub-setting was conducted on the used and adopted images. This step was conducted using the arc map 10.3 environments with the use of a boundary shape file of the study area.

For image resampling, the nearest neighbour approach is widely adopted in different kinds of applications of remote sensing. The nearest neighbour adopts the pixel's digital value in the original image, which is the nearest location to a new pixel location in the corrected image. This approach tries to outcomes in dis-jointed or blocky image appearance. This technique gives a value to the corrected pixel from the nearest uncorrected pixel. However, a disadvantage of applying the neighbour approach is the location errors along with the linear features [33]. In this research, the low spatial resolution image of thermal band 11 has been selected for performing image resampling using the neighbour approach, and the resampling process was conducted using ENVI 5.3 Environment software. Figures 3-a to 3-d show all four of the corrected satellite images after removing all kinds of noise and resampling. Figures 4-a to 4-d illustrate a subsetted of all four satellite images of Baghdad.

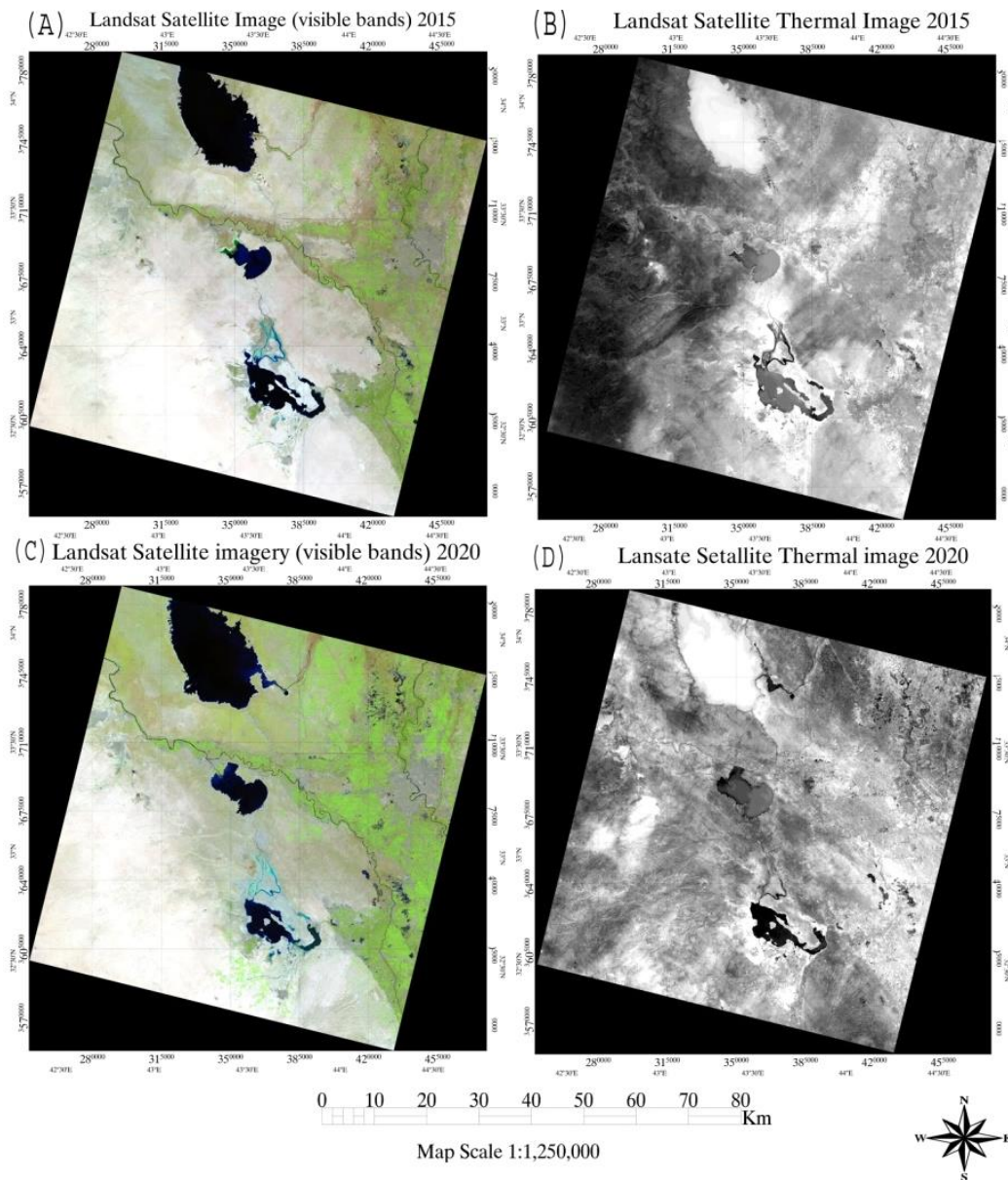


Figure 3. All the corrected satellite images, free of all the noise: (A) the corrected visible Landsat-8 satellite image of the year 2015; (B) the corrected thermal Landsat-8 satellite image of the year 2015; (C) the corrected visible Landsat-8 satellite image of the year 2020; (D) the corrected thermal Landsat satellite image of the year 2020.

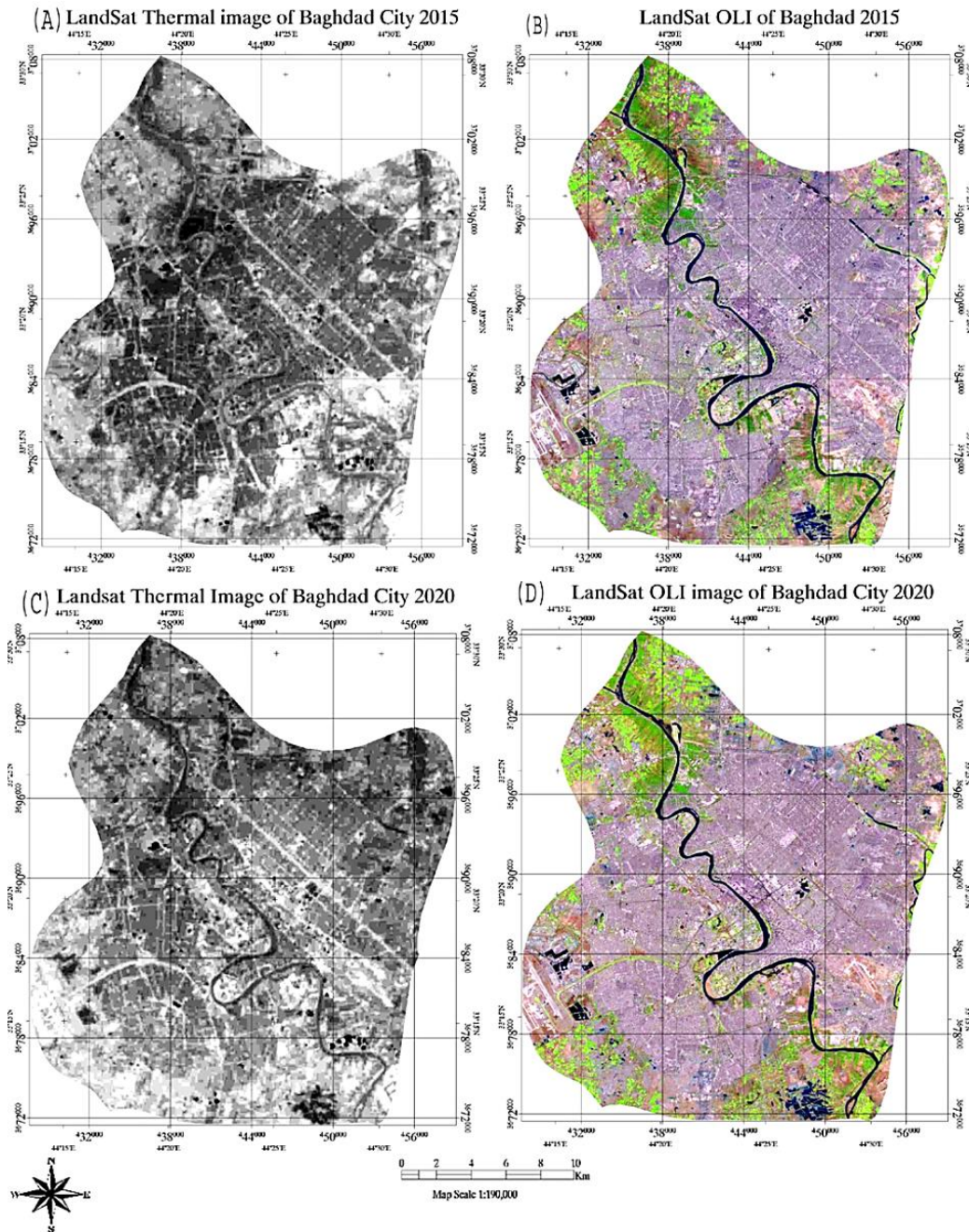


Figure 4. The subset of the satellite images are: (A) the corrected visible Landsat satellite image of the year 2015; (B) the corrected thermal Landsat satellite image of the year 2015; (C) the corrected visible Landsat satellite image of the year 2020; (D) the corrected thermal Landsat satellite image of the year 2020.

3- The Pan-sharpening Processing

Images fusion using pan-sharpening algorithms applied to different images that have different resolutions will give the advantage to improve and enhance both quantitative and visual interpretation during image analysis [34]. In this study, the thermal Landsat-8 band (11) was combined and integrated with the visible Landsat-8 image bands; Red, Green, and Blue bands of the OLI sensor, using the GS pan-sharpening technique [35]. This algorithm reveals more efficient outputs compared with other conventional pan-sharpening techniques. For instance, color normalized (CN) and principal component (PC) [36]. The GS approach is an effective algorithm for conducting integration and fusion of different image resolutions. Six fused images were created in this study using thermal data and all three visible image bands for 2015 and 2020, respectively. Then the band combinations were processed to create six false-colored images by combining the three visible bands with pan-sharpening images of 2015 and 2020 to increase the recognition of features located in the images. Table 3 shows the six false-colored images for 2015 and 2020. Secondly, the six fused images were adopted for further processing and analysis by applying three different classifiers to investigate and examine the effectiveness of combining the Landsat thermal TIRS images for the LC changes monitoring. Figures 5-a to 5-f reveal the results of the fused thermal and visible satellite images.

Table 3. The false images of using pan-sharpening bands and the visible bands of 2015 and 2020

Experiment No.	The combination of false colored of 2015	The combination of false colored of 2020
first,	Pan-sharpening band /Green band/Blue band	Pan-sharpening band / Green band/Blue band
second,	Red band /Pan-sharpening band /Blue	Red band/ Pan-sharpening band / Blue band
third,	Red band/ Green band / Pan-sharpening band	Red band / Green band / Pan-sharpening band

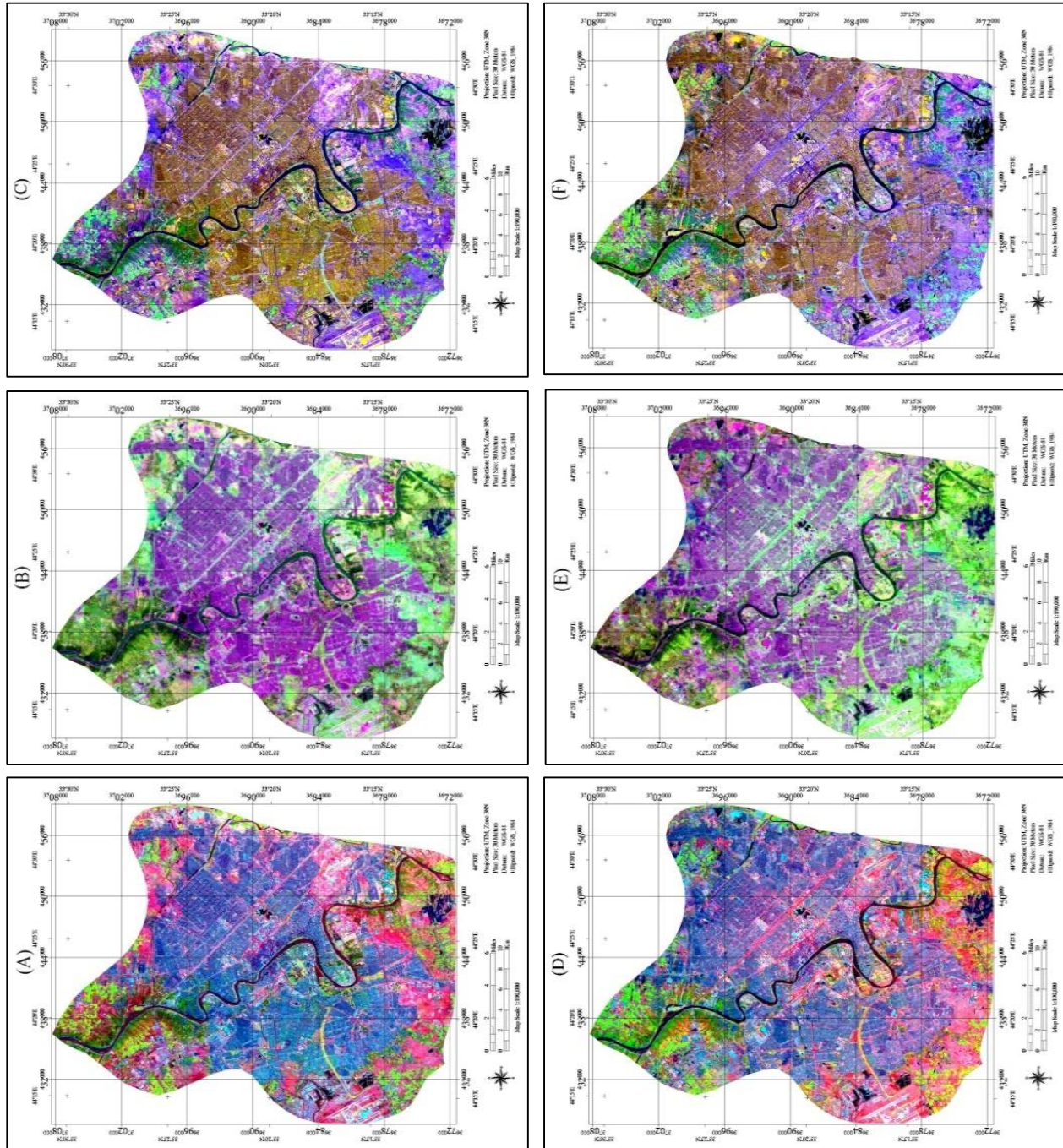


Figure 5. The false-colored images of the combination between the visible with pan-sharpening bands (A) image combination of (Pan-sharpening band / Green band/Blue band) of 2015, (B) image combining of (Red band / Pan-sharpening band/ Blue) of 2015, (C) image combining of (Red band / Green band / Pan-sharpening band) of 2015, (D) image combining of (Pan-sharpening band / Green band/Blue band) of 2020, (E) image combining of (Red band / Pan-sharpening band / Blue) of 2020, (F) image combining of (Red band /Green band/ Pan-sharpening band) of 2020.

Image interpretation is important to check out which of the combined images shown in Figures 5-a to 5-f is the most accurate and suitable to go with further processing for the next stages of this study. Regarding image visual interpretation, it is revealed that the false colored image generated by combining the bands; Red, Green, and Pan-sharpening between (Thermal and Blue) bands is the best integration and combination to make all the located objects in images more recognized as shown in Figure 5 (C & F) in images of 2015 and 2020.

4- Suitable Image Classifier Selection

For detecting and monitoring the changes in the LC using satellite image classification, many previous studies and research are discussed in the literature. Machine Learning Algorithms (MLAs) are widely used and examined [35–37]. For this study, three methods were adopted to perform image classification: ANN, MH, and ML on both the visible and combined satellite imagery to generate 12 LC thematic maps to investigate the effectiveness of thermal data and determine which algorithm is the best for detecting the LC changes over the time period from 2015 to 2020 in the Baghdad city. Many factors were considered in this research:

- The remote sensing images' spatial-resolution,
- Different sources of the images,
- Image classification approaches,
- The availability of image classification software should be accounted for when choosing a classification method [28].

The question that needs to answer in this research is which image classification technique is the most suitable and accurate for Baghdad city. The applied classifiers are:

4-1- Artificial Neural Approach

The ANN approach is one of the approaches that have been selected to perform this study. It is known as one of the non-parametric algorithms that are widely adopted for image classification [38, 39]. The ANN approach was applied to the images with the use of the ENVI 5.3 environment software. The method weights employed a uniform distribution. The applied learning rates were (0.001) and (100) for both the output and the hidden layer. Furthermore, the stopping criterion is equal to 0.001. The activation was selected to be logistic; the contribution of the training threshold is 0.9000, the training rate is equal to 0.2000, the training momentum is equal to 0.9000, the number of the hidden layer was equal to 1, and 1000 as the training iterations number.

4-2- Mahalanobis Distance Classifier

The MH method is well-known as a supervised pixel-based classifier; it was created by an Indian researcher in the 1930s. The MH method is a parametric technique and is widely adopted for the classification of different satellite and remotely sensed images. It does not need to assume the applied data to get a normal distribution. The MH algorithm works between two points in the dataset [40, 41]. In mathematical terms, the MH method is equal to a method of the Euclidean Distance method (ED). When a unit of the matrix is represented as a covariance matrix. The MH algorithm is a small value that will increase an observation's chance of being close to a center group. For each feature vector, the MH (D_k^2) towards class means is determined as Equation 1 [42]:

$$D_k^2 = \langle x_i - \bar{x}_k \rangle^T S_k^{-1} \langle x_i - \bar{x}_k \rangle \quad (1)$$

where, x_i is represented an image vector pixel, \bar{x}_k has represented a sample of the mean vector (MV) regarding (kth) class. S_k^{-1} is represented by the Variance and Covariance Matrix of class (i). The (T) is represented the matrix transpose.

4-3- Maximum Likelihood Approach

The third classifier adopted in this study was the ML technique. The ML method is well known for conducting image classification techniques [43, 44]. This method was assigned to give accurate image classification results [45, 46]. The ML method is applied to determine the weighted distance and likelihood (Z) that relate to unknown measures of a vector (Y) that relate to unknown classes. The ML method works regarding the original Bayesian Equation 2 as shown below [47, 48]:

$$Z = \ln(at) - [0.5\ln(|covt|)] - [0.5(Y - At)T(covt - 1)(Y - At)] \quad (2)$$

where (at) is represented as the mean vector of the target class [t], (at) is also presented as the percent of probability, and (covt) is represented as a covariance matrix of class (t). The |covt| is represented a (covt) determinant, A (covt-1) is represented the inversed of the (covt). Ln is represented as a natural logarithm function, and AT is a translocation function. The MD, ANN, and ML methods were adopted on the images of the Landsat, pan-sharpened, combined images of OLI and TIRS of 2015 and 2020 to generate twelve maps for detection of the changes of LC. The study area was classified into six different classes; Urbanization Area, Water bodies Areas, Plantation Area, Soil Area, Clay Area, and Asphalt Roads.

4-4- Selection of Testing and Training sites

Training samples' number and size play a big role in image classification accuracy; the best selection of training sites is a pre-requisite for producing an accurately classified image [49]. As referenced in previous works [50, 51], the size of training samples should not be fewer than 10–30 pixels for each class. Furthermore, this research is adopting image interpretation with the use of Google Earth for collecting the training and testing that relate to each of the six defined classes. The collected training samples were divided into two categories: the first was employed for conducting image classification with about 70% of the samples, and the second was adopted for conducting the validation of image classification results with about 30% of the samples [34, 52]. Finally, the LC maps were generated by using three different classification methods. In this study, the size of the sites for both visible and combined images was greater than 300 pixels. However, only 200 pixels for each class (water bodies and soil area) were collected because the river is too small.

4-5- Results Validation

The Confusion matrix was applied to validate the results of each classification to produce the overall accuracy (OA), producer accuracy (PA), user's accuracy (UA), and Kappa coefficient (KC) as reported by Nappo et al. [52]. In this study, the equations of validation method are illustrated below:

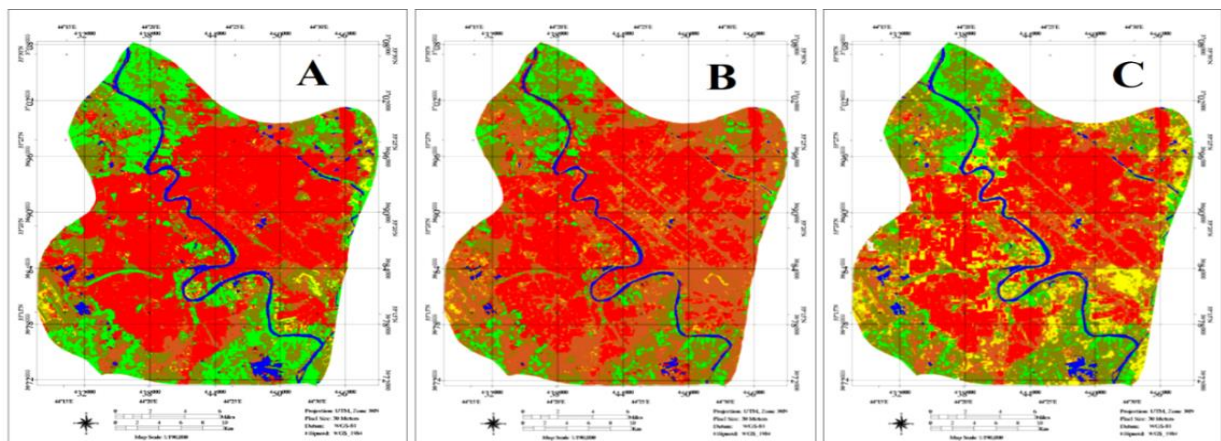
$$OA = \frac{\sum_{i=1}^c n_{ij}}{n} \quad (3)$$

$$KC = \frac{\sum_{i=1}^c n_{ii} - \sum_{i=1}^c n_i + n - i}{n^2 - \sum_{i=1}^c n_i + n + i} \quad (4)$$

where (n) is represented the pixels' total number, the (nij) is represented the total number of the classified pixels, the (ni) is represented an instances number, and the label (i) of the classified into the label (j).

5- Results and Discussion

Three algorithms are adopted to examine the effectiveness of employing the thermal images to map the LC change detection in the study area. Twelve maps were generated for this study from the images of 2015 and 2020. It divides into two categories; the first one has six LC maps created by adopting the MD, ANN, and ML classifiers. Figures 6-A to 6-C show the maps produced from conducting image classification on the Landsat satellite visible images of 2015. Figures 6-D to 6-F show the maps produced by conducting image classification techniques on the pan-sharpening and combination of the visible Landsat satellite with thermal images in 2015. However, the second one has six LC maps that were generated by employing the same classification methods. Figures 7-A to 7-C show the generated maps by conducting image classification on the visible Landsat images of 2020. However, Figures 7-D to 7-F indicate the maps created by performing image classification on the pan-sharpening and combining visible and thermal images in 2020. Figures 6 (A, B, and C) and 7 (A, B, and C) show the maps resulting from the image classification of the visible images of 2015 and 2020, respectively. The patterns cannot be observed visually in the classes Soil Area, Clay Area, and Roads. On the other hand, other patterns and classes are recognizable. However, Figures 6 (D, E, and F) and 7 (D, E, and F) show the produced maps from the image classification of the combination and pan-sharpening thermal and visible images of 2015 and 2020, respectively. It is clear that the patterns of each class can be observed, and it provides more information, and the Soil Area, Clay Area and Road patterns are easy to observe. Tables 4 and 5 show the classification results for each image: OA, PA, and UA, respectively.



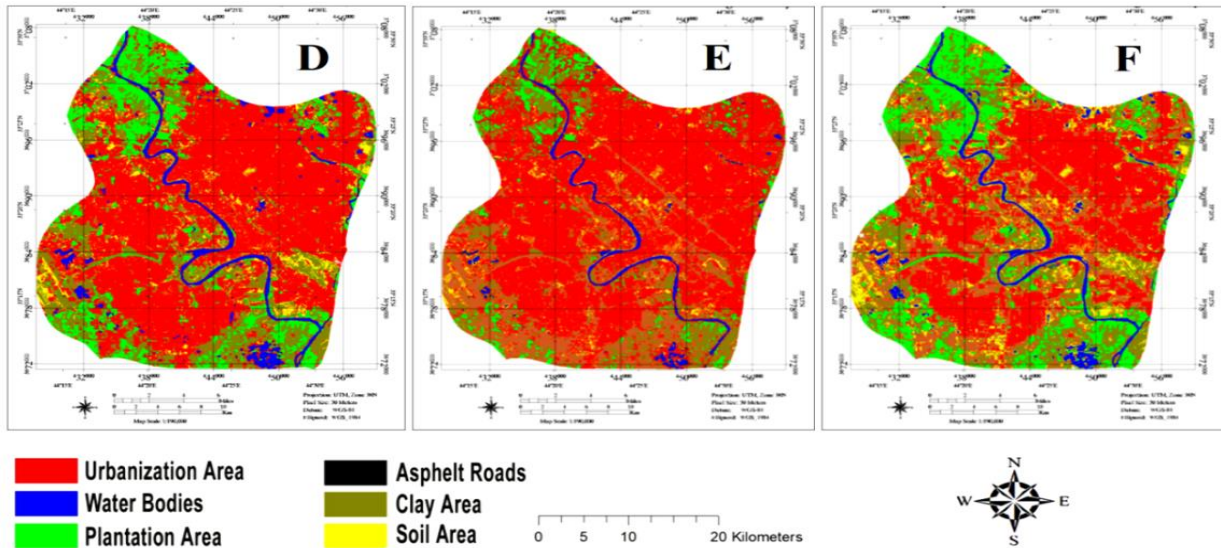


Figure 6. The classified images used the visible images and pan-sharpening images with the combination of the visible and thermal images of 2015; (A) the ANN method on the visible images; (B) the MD method on the visible datasets; (C) the ML method on the visible images; (D) the ANN method on the pan-sharpening with combination datasets; (E) the MD method on the pan-sharpening with combination datasets, and (F) the ML technique on the pan-sharpening with combination datasets.

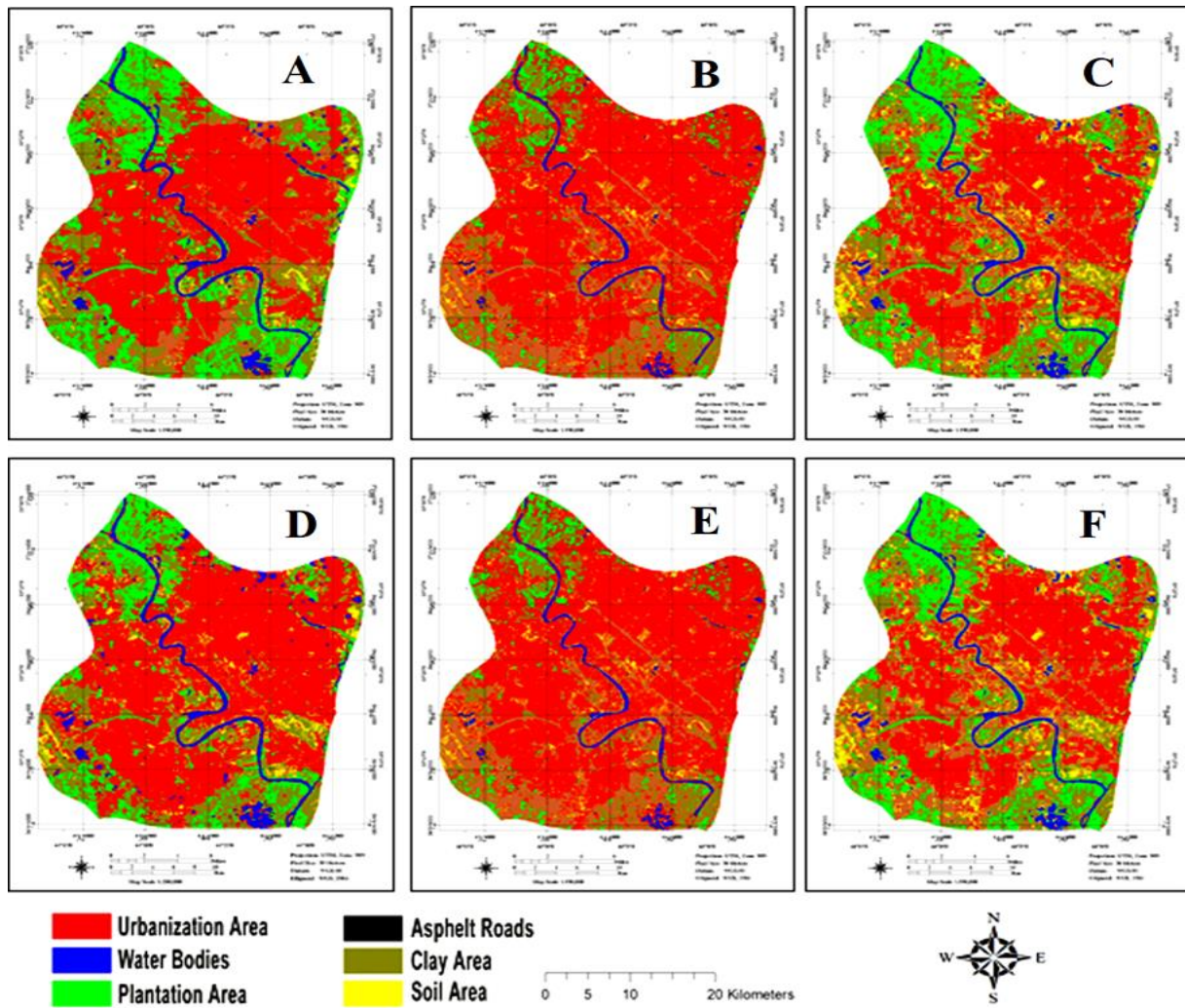


Figure 7. The classified images used the visible datasets and the pan-sharpening with a combination of the visible and thermal data of 2020; (A) the ANN algorithm on the visible images; (B) the MD algorithm on the visible images; (C) the ML algorithm on the visible images; (D) the ANN algorithm on the pan-sharpening with the combination images; (E) the MD algorithm on the pan-sharpening with the combination images; and (F) the ML algorithm on the pan-sharpening with the combined images.

Table 4. OAs and KCs of the MD, ANN, and ML approaches applied to the Landsat images of 2015 and 2020

No.	Years	Methods	Landsat Satellite Images (Visible Bands)		Combination of Thermal and Visible Landsat Satellite Image Bands	
			OA (%)	KC	OA (%)	KC
1		ANN	90.31	0.90	96.31	0.94
2	2015	MD	88.64	0.85	94.74	0.93
3		ML	89.00	0.87	95.11	0.94
4		ANN	92.25	0.91	98.40	0.97
5	2020	MD	89.49	0.88	94.34	0.93
6		ML	90.78	0.90	96.23	0.95

Table 5. Reveals Producer and User accuracies of the MD, ANN, and ML approaches of combined images of 2015 and 2020

Classes	ANN of 2015 combination		ANN of 2020 combination		MD of 2015 combination		MD of 2020 combination		ML of 2015 combination		ML of 2020 combination	
	PA	UA	PA	UA	PA	UA	PA	UA	PA	UA	PA	UA
Urban area	98.04	96.73	99.60	98.35	94.36	97.54	96.33	98.24	93.29	93.83	93.65	93.65
Vegetation	98.17	91.31	99.76	99.76	94.66	96.43	95.73	94.23	94.33	93.69	94.76	94.51
Water bodies	98.86	99.48	99.37	100.0	95.65	96.23	96.53	93.15	93.34	93.85	94.20	95.94
Soil area	66.55	96.12	95.80	96.45	83.91	91.54	84.71	92.65	92.38	93.53	95.32	95.71
Roads	59.00	59.27	90.84	91.74	78.34	44.66	79.04	43.43	51.33	51.36	92.48	80.88
Clay area	77.54	81.64	98.41	96.88	85.46	87.95	86.66	88.89	96.84	94.44	98.94	95.90

5-1- Result Validation

There are about twelve generated thematic maps that need to be evaluated using the collected testing samples from Google Earth exploration and image interpretation. These samples were involved in the process of the confusion matrix. Since both the OA and KC are widely adopted for the assessment of image classification results. Therefore, both the OA and KC were determined to validate the produced maps as referenced by Deng and Wu (2013) [50]. Furthermore, a statistical comparison was performed to test the performance of the applied algorithms to map the Baghdad city changes for the period between 2015 to 2020. A statistical result illustrates in Table 4, indicates the OA and KC of each applied method; MD, ANN, and ML between 2015 and 2020 from using multi-spectral images of the Landsat satellite system. Moreover, it also shows the OA and KC of the same classification approaches that were applied to the combined images of the integration between the Landsat OLI (visible) and TIRS (thermal) images of 2015 and 2020. Table 4 indicates that the results of applying the ANN algorithm in 2015 have the highest values of the OA and KC at about 90.31% and 0.90, respectively. However, the result of the MD approach has the lowest values of OA and KC, about 88.64% and 0.85, respectively, compared to other image classifications. The results reveal that both the soil area and road classes are still very difficult to observe in all the produced LC thematic maps. However, the image classification of the integration and combining of images reveals the beauty of applying the ANN algorithm. The ANN approach also recorded the highest OA and KC values of about 96.31% and 0.94, respectively. The OA value of the ANN method increased by about 6%. While the ML algorithm recorded a result higher than the got by applying the MD method. The ML classifier has a value of OA and KC of about 95.11% and 0.94, respectively.

A statistical result in Table 4 of 2020 indicates that the ANN approach has the highest values of OA and KC at 92.25% and 0.91, respectively. Moreover, the MD technique creates a map that has the lowest OA and KC values at 89.49% and 0.88, respectively. On the other hand, the values of OA and KC of the image classification results produced from image integration and combinations in 2020 between the thermal and visible datasets reveal more accurate outcomes. The ANN approach also records the highest values of OA and KC with about 98.40% and 0.97, respectively. Meanwhile, the ML classifier records accuracy levels higher than those obtained from applying the MD approach, compared with the image classification in 2020 generated by using only the Landsat visible image. The ML method has OA and KC values of about 96.23% and 0.95, respectively. Regarding the all obtained results of the twelve image classifications, it is seen that the images combined and integrated with the thermal bands enhance and improve the value of the OA by about 6% for all the applied and employed classifiers; ANN, ML, and MD on the datasets. Table 4 also indicates the superior performance of applying the ANN method on images combined of thermal and visible using bands; Red, Green, and Pan-sharpening, for mapping the change detection of the LC and compared with another used method.

Therefore, the ML classifier has performed slightly better than the MD classifier for monitoring the changes in the LC. However, the ANN technique has an advantage over the ML method in that the classes of all classified images can be recognized. Table 3 indicates the effectiveness of applying the thermal datasets to detect the LC changes and it reveals a superiority with a higher value of the OA than the used of the classified visible image from following the arranging of

these bands; Red, Green, and Blue pan-sharpening with the thermal band (11). Furthermore, Table 5 and Figure 8 reveal the PA and UA for all classes of the classified combined images between the thermal (band 11) and the visible bands by applying the MD, ANN, and ML methods, and they reveal how much the improvements and enhancement of the PA and UA. It is obvious that the PA and UA results have increased dramatically.

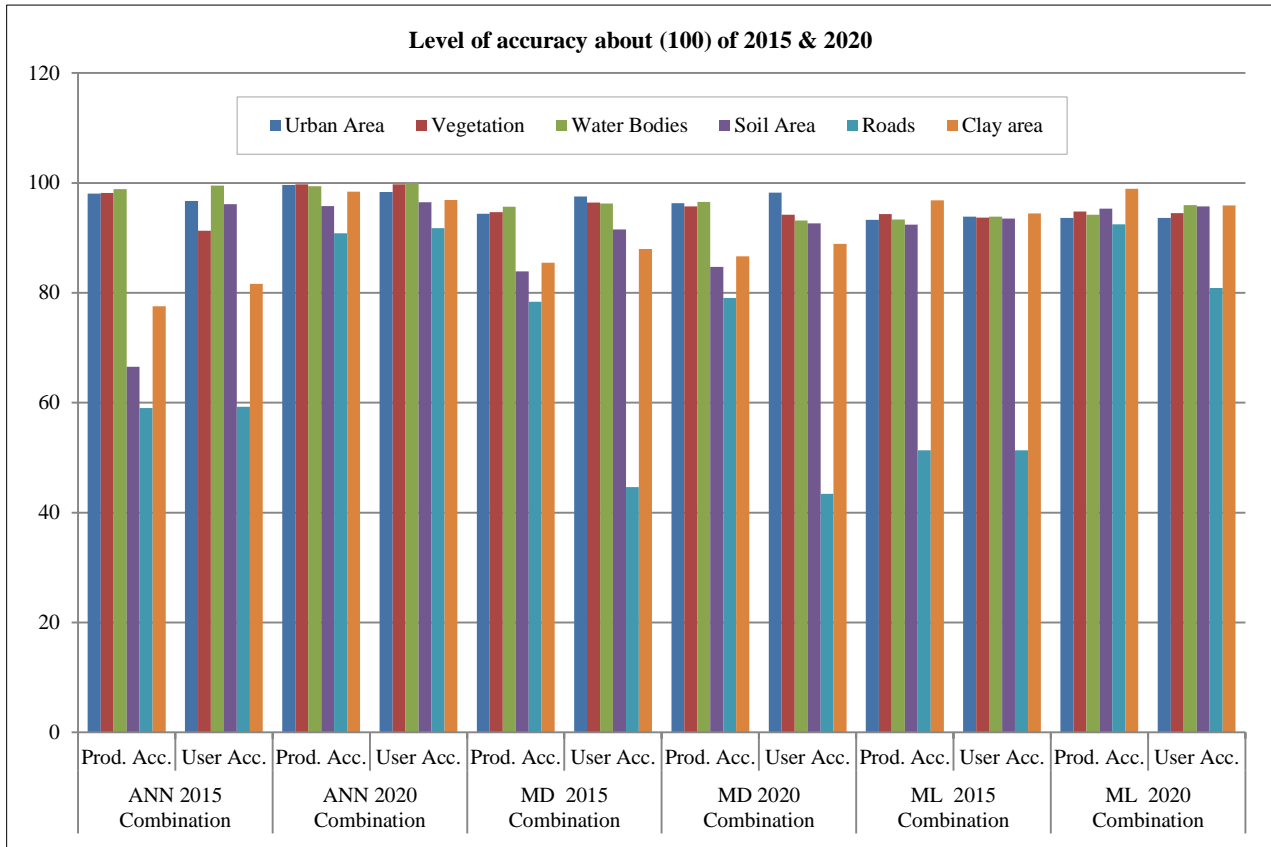


Figure 8. PA and UA of all classes of the integrated and classified thermal images of 2015 and 2020 by using classifiers: MD, ANN, and ML algorithms

For soil area, roads, and clay area classes, the ANN accuracy of the 2015 images was compared to the ANN accuracy of the 2020 images. Soil area PA increased from (66.55) to about (95.80), and the PA of the Roads class in 2015 was about (59.00). But in 2020, there is a steep increase in this value to record a value of about 90.84, which decreases the misclassification between the maps and improves and enhances the OA to be higher than before, as illustrated in Table 3. On the other hand, the clay area achieves a PA value of about 77.54. Furthermore, the clay area of 2020 has increased slightly to a record of about 96.88. Therefore, by comparing the outcomes of Table 4, it can be concluded that the highest values of the PA and UA were generated by applying the ANN algorithm compared to other image classification methods, and it gives the most accurate results for the LC map of the Baghdad city. In Figure 8, the PA and UA columns can illustrate the values of each method compared to another. Therefore, it was concluded that accurate LC estimating maps could be obtained by applying the GS-sharpening algorithm between datasets of the thermal band (11) of the TIRS sensor and the Landsat OLI visible bands, then generating a false-colored image from the combination of the following bands: Red, Green and Pan-sharpening and then adopting the ANN method to conduct imagery classification.

Hashim et al. (2021) applied the SVM method to low-spatial-resolution Landsat-8 OLI multi-spectral datasets; they got overall accuracy and kappa coefficients of 90.61% and 0.89, respectively [22]. Another study conducted by Dibs et al. [34] adopted different fusion methods using a variety of classifiers to classify the satellite images. However, both Hashim et al. [22] and Dibs et al. [34] studied the same area, but they got less accuracy than the proposed method for this study. So, the results of this research indicate that the high performance of using and applying the ANN method with integrating and combining both the thermal and visible images of the Landsat OLI and TIRS sensors in the CD between different periods. Regarding Section 2.1, the area of the research area is about 2260.2 km², Figure 8 and Table 6 represent the results of all the changes related to the study area classes. The statistical results, summarized in Table 6, reveal the percent of increasing and decreasing values for each class for both 2015 and 2020. However, Figure 9 shows those changes in the unit of (Km²), and the most changes occur in the class of urban area, it was about 1372.619 km² in 2015. Then, it increased to about 6.57 % in 2020 to a record about 1521.115 km². This increment achieved about 148.496 Km².

Furthermore, the results show successful detection of the changes in the class of the vegetation area; the change was about 356.434 km² in 2015, and it began to decrease to become about 221.5 Km². In other words, it means that it is lost by about -05.97%, which is equal to 134.934 km² of the area of this class. The increase in the urban area and the decrease in the vegetation area could be explained to be effective by the people's immigration periods between 2015 to 2020 from other surrounding cities to Baghdad city. The total Water Bodies Area is slightly increased from (128.153 Km²) in 2015 to about (132.674 Km²) in 2020, the increment of Water Bodies Area about +0.20% and that is equal to 4.52 Km², the increment occurs, because of the heavy rain during 2020 after the long dry season, that start from 2015-2019. Moreover, the results show that the Soil Area reduced from (161.152 Km²) in 2015 to became about (124.99 km²) in 2020, there is a slightly decreasing in the class of Soil Area (-01.60 %) and that equal to (36.162 Km²) for the time between 2015 to 2020, that occurred simply because 2020 has a heavy rainy season. In 2015, and for the same reasons, it also had the rainy season, and for that, the clay area recorded a slight increment of about 118.66 Km², with an increment of about +00.10 and it being equal to 2.261 Km², the clay area in 2020 became about 120.921 Km². However, the road area in Baghdad City begins to increase from approximately 123.181 Km² in 2015 to an increment of +00.70 and be equal to 15.821 Km², to become about 139.002 Km² in 2020. This increment happens because of the development of the City Urbanization occurs between 2015 to 2020. In this research, the developed technique and procedure were significantly better than all the applied conventional techniques to map the change detection in the LC [53].

Table 6. Results of the LC classes using the combined images of 2015 and 2020

No.	Classes	Percent (%) of the ANN in 2015	Percent (%) of the ANN in 2020	Differences in (%)
1	urban area	60.73	67.30	+06.57
2	vegetation area	15.77	09.80	-05.97
3	water bodies	05.67	05.87	+00.20
4	soil area	07.13	05.53	-01.60
5	roads	05.45	06.15	+00.70
6	wet clay area	05.25	05.35	+00.10

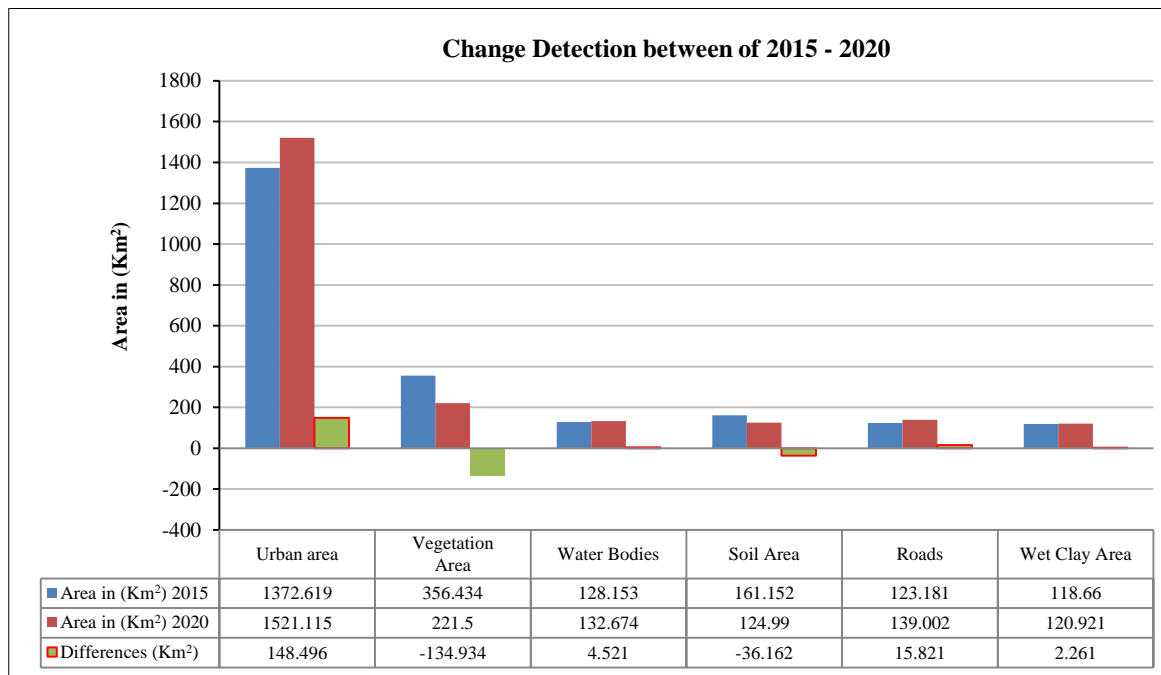


Figure 9. Change detection of each class of the study area between 2015 and 2020

6- Conclusion

Monitoring and detection of LC changes are widely tested and examined for different applications, such as ecological, environmental, and hydrological ones. The thermal dataset provides valuable information to improve and enhance change detection outcomes. However, using only the visible, remotely sensed datasets will not provide good information and better results. The up-to-date changes in LC and obtaining geospatial information with highly accurate results is a difficult task to perform, especially with the availability of image classification methods and types of data that adopt and employ in last previous decades. Therefore, there is a need to perform change detection in the LC using other types of data and other techniques or methodologies to get significant outcomes. Therefore, this study investigates the integration of the thermal dataset using the GS-spectral approach and the visible dataset, and then the best-combining bands were

chosen for performing the LC change detection classification with the use of the ML, MD, and ANN algorithms to find out the best and most accurate model in terms of finding the accurate methodology and procedure for estimating the LC changes on the map of both 2015 and 2020 of Baghdad city. The results reveal that producing the LC changes with highly accurate outcomes will be with performing the pan-sharpening on thermal images with visible image bands. Suitable and reliable change detection results are assessed by applying the confusion matrix. The result indicates that the superior performance technique is applying the ANN method to the pan-sharpened image by the GS method. The ANN method outcome has the highest AO and KC values compared to other adopted methods, with OA at about 96.31% & 98.40% and the KC at about 0.94 and 0.97 for 2015 and 2020, respectively. On the other hand, the combination of thermal data with visible data enhances the amount of the AO by about 5 % and 6% for the applied classification algorithms of the Landsat OLI datasets and is better than using low spatial-resolution visible datasets alone. The outcomes show that there is significant potential for using TIRS data to detect changes in the LC. However, the limitations were just using low-spatial datasets. Future work will include examination of additional remotely sensed datasets (IKONOS, QuickBird, SPOT, and other satellite systems) and investigations of other classification methods to monitor the changes in the LC.

7- Declarations

7-1- Author Contributions

Conceptualization, H.D. and A.H.A.; methodology, H.D. and A.H.A.; software, H.D. and A.H.A.; validation, H.D., S.A.A. and N.A.A.; investigation, H.D., and N.A.A.; data curation, H.D. and A.H.A.; writing—original draft preparation, H.D., A.H.A., S.A.A. and N.A.A.; visualization, S.A.A. and N.A.A.; project administration, N.A.A. All authors have read and agreed to the published version of the manuscript.

7-2- Data Availability Statement

The data presented in this study are available on request from the corresponding author.

7-3- Funding

The authors received no financial support for the research, authorship, and/or publication of this article.

7-4- Acknowledgements

The authors also would like to express their thankfulness to the AL-Qasim Green University, Al-Mustaqbal University College (Iraq), and Lulea University of Technology (Sweden) for the support provided to accomplish this study.

7-5- Institutional Review Board Statement

Not applicable.

7-6- Informed Consent Statement

Not applicable.

7-7- Conflicts of Interest

The authors declare that there is no conflict of interest regarding the publication of this manuscript. In addition, the ethical issues, including plagiarism, informed consent, misconduct, data fabrication and/or falsification, double publication and/or submission, and redundancies have been completely observed by the authors.

8- References

- [1] Dibs, H. (2018). Comparison of derived Indices and unsupervised classification for AL-Razaza Lake dehydration extent using multi-temporal satellite data and remote sensing analysis. *ARPN Jouyrnal of Engineering and Applied Sciences*, 13(24), 9495-95038.
- [2] Hasab, H. A., Jawad, H. A., Dibs, H., Hussain, H. M., & Al-Ansari, N. (2020). Evaluation of Water Quality Parameters in Marshes Zone Southern of Iraq Based on Remote Sensing and GIS Techniques. *Water, Air, and Soil Pollution*, 231(4). doi:10.1007/s11270-020-04531-z.
- [3] Dibs, H., & Al-Hedny, S. (2019). Detection wetland dehydration extent with multi-temporal remotely sensed data using remote sensing analysis and GIS techniques. *International Journal of Civil Engineering and Technology*, 10, 143-154.
- [4] Hayder Dibs, Shattri Mansor, Noordin Ahmad, Biswajeet Pradhan, & Nadhir Al-Ansari. (2020). Automatic Fast and Robust Technique to Refine Extracted SIFT Key Points for Remote Sensing Images. *Journal of Civil Engineering and Architecture*, 14(6), 339–350. doi:10.17265/1934-7359/2020.06.005.

- [5] Abdalkadhum Aljanbi, A. J., Dibs, H., & Alyasery, B. H. (2020). Interpolation and statistical analysis for evaluation of global earth gravity models based on GPS and orthometric heights in the middle of Iraq. *Iraqi Journal of Science*, 61(7), 1823–1830. doi:10.24996/ij.s.2020.61.7.31.
- [6] Dibs, H., Mansor, S., Ahmad, N., & Pradhan, B. (2014). Registration model for near-equatorial earth observation satellite images using automatic extraction of control points. *International Conference 2014 - International Systems Group (ISG), Rome, Italy*.
- [7] Dibs, H., Al-Hedny, S., & Karkoosh, H. A. (2018). Extracting Detailed Buildings 3D Model with Using High Resolution Satellite Imagery by Remote Sensing and GIS Analysis; Al-Qasim Green University a Case Study. *International Journal of Civil Engineering and Technology*, 9(7), 1097-1108.
- [8] Ramos-Bernal, R. N., Vázquez-Jiménez, R., Romero-Calcerrada, R., Arrogante-Funes, P., & Novillo, C. J. (2018). Evaluation of unsupervised change detection methods applied to landslide inventory mapping using ASTER imagery. *Remote Sensing*, 10(12). doi:10.3390/rs10121987.
- [9] Cao, G., Zhou, L., & Li, Y. (2016). A new change-detection method in high-resolution remote sensing images based on a conditional random field model. *International Journal of Remote Sensing*, 37(5), 1173–1189. doi:10.1080/01431161.2016.1148284.
- [10] Asokan, A., & Anitha, J. (2019). Change detection techniques for remote sensing applications: a survey. *Earth Science Informatics*, 12(2), 143–160. doi:10.1007/s12145-019-00380-5.
- [11] Lv, Z., Liu, T., Shi, C., Benediktsson, J. A., & Du, H. (2019). Novel Land Cover Change Detection Method Based on k-Means Clustering and Adaptive Majority Voting Using Bitemporal Remote Sensing Images. *IEEE Access*, 7, 34425–34437. doi:10.1109/ACCESS.2019.2892648.
- [12] Dibs, H., Mansor, S., Ahmad, N., & Pradhan, B. (2015). Band-to-band registration model for near-equatorial Earth observation satellite images with the use of automatic control point extraction. *International Journal of Remote Sensing*, 36(8), 2184–2200. doi:10.1080/01431161.2015.1034891.
- [13] Halder, S., Tiwari, Y. K., Valsala, V., Sijikumar, S., Janardanan, R., & Maksyutov, S. (2022). Benefits of satellite XCO₂ and newly proposed atmospheric CO₂ observation network over India in constraining regional CO₂ fluxes. *Science of the Total Environment*, 812, 151508. doi:10.1016/j.scitotenv.2021.151508.
- [14] Xiao, P., Yuan, M., Zhang, X., Feng, X., & Guo, Y. (2017). Cosegmentation for Object-Based Building Change Detection from High-Resolution Remotely Sensed Images. *IEEE Transactions on Geoscience and Remote Sensing*, 55(3), 1587–1603. doi:10.1109/TGRS.2016.2627638.
- [15] Dibs, H., Mansor, S., Ahmad, N., & Al-Ansari, N. (2020). Simulate New Near Equatorial Satellite System by a Novel Multi-Fields and Purposes Remote Sensing Goniometer. *Engineering*, 12(06), 325–346. doi:10.4236/eng.2020.126026.
- [16] Abdullah, A. Y. M., Masrur, A., Gani Adnan, M. S., Al Baky, M. A., Hassan, Q. K., & Dewan, A. (2019). Spatio-temporal patterns of land use/land cover change in the heterogeneous coastal region of Bangladesh between 1990 and 2017. *Remote Sensing*, 11(7), 790. doi:10.3390/rs11070790.
- [17] Dibs, H., Hasab, H. A., Jaber, H. S., & Al-Ansari, N. (2022). Automatic feature extraction and matching modelling for highly noise near-equatorial satellite images. *Innovative Infrastructure Solutions*, 7(1). doi:10.1007/s41062-021-00598-7.
- [18] Hegazy, I. R., & Kaloop, M. R. (2015). Monitoring urban growth and land use change detection with GIS and remote sensing techniques in Daqahlia governorate Egypt. *International Journal of Sustainable Built Environment*, 4(1), 117–124. doi:10.1016/j.ij.sbe.2015.02.005.
- [19] Rawat, J. S., & Kumar, M. (2015). Monitoring land use/cover change using remote sensing and GIS techniques: A case study of Hawalbagh block, district Almora, Uttarakhand, India. *Egyptian Journal of Remote Sensing and Space Science*, 18(1), 77–84. doi:10.1016/j.ejrs.2015.02.002.
- [20] Vázquez-Jiménez, R., Romero-Calcerrada, R., Novillo, C. J., Ramos-Bernal, R. N., & Arrogante-Funes, P. (2017). Applying the chi-square transformation and automatic secant thresholding to Landsat imagery as unsupervised change detection methods. *Journal of Applied Remote Sensing*, 11(1), 016016. doi:10.1117/1.jrs.11.016016.
- [21] Kwarteng, A. Y., & Chavez Jr, P. S. (1998). Change detection study of Kuwait City and environs using multi-temporal Landsat Thematic Mapper data. *International Journal of Remote Sensing*, 19(9), 1651-1662. doi:10.1080/014311698215162.
- [22] Hashim, F., Dibs, H., & Jaber, H. S. (2021). Applying Support Vector Machine Algorithm on Multispectral Remotely sensed satellite image for Geospatial Analysis. *Journal of Physics: Conference Series*, 1963(1). doi:10.1088/1742-6596/1963/1/012110.
- [23] International Association of Assessing Officers Technical Standards Committee. (2014). Guidance on international mass appraisal and related tax policy. *Journal of Property Tax Assessment & Administration*, 11(1), 5-33.
- [24] Yang, C., He, X., Yan, F., Yu, L., Bu, K., Yang, J., Chang, L., & Zhang, S. (2017). Mapping the influence of land use/land cover changes on the urban heat island effect-A case study of Changchun, China. *Sustainability (Switzerland)*, 9(2). doi:10.3390/su9020312.

- [25] Maulik, U., & Chakraborty, D. (2017). Remote Sensing Image Classification: A survey of support-vector-machine-based advanced techniques. *IEEE Geoscience and Remote Sensing Magazine*, 5(1), 33–52. doi:10.1109/MGRS.2016.2641240.
- [26] Dibs, H., & Hussain, T. H. (2018). Estimation and Mapping the Rubber Trees Growth Distribution using Multi Sensor Imagery with Remote Sensing and GIS Analysis. *Journal of University of Babylon for Pure and Applied Sciences*, 26(6), 109-123.
- [27] Fahad, K. H., Hussein, S., & Dibs, H. (2020). Spatial-Temporal Analysis of Land Use and Land Cover Change Detection Using Remote Sensing and GIS Techniques. *IOP Conference Series: Materials Science and Engineering*, 671(1), 012–046. doi:10.1088/1757-899X/671/1/012046.
- [28] Dibs, H., Hasab, H. A., Al-Rifaie, J. K., & Al-Ansari, N. (2020). An Optimal Approach for Land-Use / Land-Cover Mapping by Integration and Fusion of Multispectral Landsat OLI Images: Case Study in Baghdad, Iraq. *Water, Air, & Soil Pollution*, 231(9). doi:10.1007/s11270-020-04846-x.
- [29] Wang, M., Wan, Y., Ye, Z., & Lai, X. (2017). Remote sensing image classification based on the optimal support vector machine and modified binary coded ant colony optimization algorithm. *Information Sciences*, 402, 50–68. doi:10.1016/j.ins.2017.03.027.
- [30] Prieto-Amparan, J. A., Villarreal-Guerrero, F., Martinez-Salvador, M., Manjarrez-Domínguez, C., Santellano-Estrada, E., & Pinedo-Alvarez, A. (2018). Atmospheric and radiometric correction algorithms for the multitemporal assessment of grasslands productivity. *Remote Sensing*, 10(2), 219. doi:10.3390/rs10020219.
- [31] Zhang, J., Dong, W., Wang, J. X., & Liu, X. N. (2014). A method to enhance the fog image based on dark object subtraction. *Applied Mechanics and Materials*, 543–547, 2484–2487. doi:10.4028/www.scientific.net/AMM.543-547.2484.
- [32] Roy, D. P., Li, J., Zhang, H. K., & Yan, L. (2016). Best practices for the reprojection and resampling of Sentinel-2 Multi Spectral Instrument Level 1C data. *Remote Sensing Letters*, 7(11), 1023–1032. doi:10.1080/2150704X.2016.1212419.
- [33] Hashim, F., Dibs, H., & Jaber, H. S. (2022). Adopting Gram-Schmidt and Brovey Methods for Estimating Land Use and Land Cover Using Remote Sensing and Satellite Images. *Nature Environment and Pollution Technology*, 21(2), 867–881. doi:10.46488/NEPT.2022.v21i02.050.
- [34] Dibs, H., Hasab, H. A., Mahmoud, A. S., & Al-Ansari, N. (2021). Fusion Methods and Multi-classifiers to Improve Land Cover Estimation Using Remote Sensing Analysis. *Geotechnical and Geological Engineering*, 39(8), 5825–5842. doi:10.1007/s10706-021-01869-x.
- [35] Dibs, H., Idrees, M. O., & Alsahin, G. B. A. (2017). Hierarchical classification approach for mapping rubber tree growth using per-pixel and object-oriented classifiers with SPOT-5 imagery. *Egyptian Journal of Remote Sensing and Space Science*, 20(1), 21–30. doi:10.1016/j.ejrs.2017.01.004.
- [36] Nazmfar, H., & Jafarzadeh, J. (2018). Classification of Satellite Images in Assessing Urban Land Use Change Using Scale Optimization in Object-Oriented Processes (A Case Study: Ardabil City, Iran). *Journal of the Indian Society of Remote Sensing*, 46(12), 1983–1990. doi:10.1007/s12524-018-0850-7.
- [37] Xu, K., Tian, Q., Yang, Y., Yue, J., & Tang, S. (2019). How up-scaling of remote-sensing images affects land-cover classification by comparison with multiscale satellite images. *International Journal of Remote Sensing*, 40(7), 2784–2810. doi:10.1080/01431161.2018.1533656.
- [38] Mohan, B.S.S., Sekhar, C.C. (2012). Class-Specific Mahalanobis Distance Metric Learning for Biological Image Classification. *Image Analysis and Recognition. ICIAR 2012. Lecture Notes in Computer Science*, 7325, Springer, Berlin, Germany. doi:10.1007/978-3-642-31298-4_29.
- [39] Fu, G., Liu, C., Zhou, R., Sun, T., & Zhang, Q. (2017). Classification for high resolution remote sensing imagery using a fully convolutional network. *Remote Sensing*, 9(5), 498. doi:10.3390/rs9050498.
- [40] Tang, Y., Zhang, F., Engel, B. A., Liu, X., Yue, Q., & Guo, P. (2020). Grid-scale agricultural land and water management: A remote-sensing-based multiobjective approach. *Journal of Cleaner Production*, 265, 121792. doi:10.1016/j.jclepro.2020.121792.
- [41] Wójtowicz, M., Wójtowicz, A., & Piekarczyk, J. (2016). Application of remote sensing methods in agriculture. *Communications in Biometry and Crop Science*, 11(1), 31-50.
- [42] Sharma, A., Liu, X., Yang, X., & Shi, D. (2017). A patch-based convolutional neural network for remote sensing image classification. *Neural Networks*, 95, 19–28. doi:10.1016/j.neunet.2017.07.017.
- [43] Hopkins, P. (1988). Assessment of Thematic Mapper Imagery for Forestry Application under Lake States Conditions. *Photogrammetric Engineering and Remote Sensing*, 54(1), 61-68.
- [44] Liu, B., Yu, X., Zhang, P., Tan, X., Yu, A., & Xue, Z. (2017). A semi-supervised convolutional neural network for hyperspectral image classification. *Remote Sensing Letters*, 8(9), 839–848. doi:10.1080/2150704x.2017.1331053.
- [45] Cavallaro, G., Riedel, M., Richerzhagen, M., Benediktsson, J. A., & Plaza, A. (2015). On Understanding Big Data Impacts in Remotely Sensed Image Classification Using Support Vector Machine Methods. *IEEE Journal of Selected Topics in Applied Earth Observations and Remote Sensing*, 8(10), 4634–4646. doi:10.1109/JSTARS.2015.2458855.

- [46] Jog, S., & Dixit, M. (2016). Supervised classification of satellite images. Conference on Advances in Signal Processing, CASP 2016, 93–98. doi:10.1109/CASP.2016.7746144.
- [47] Srivastava, P. K., Han, D., Rico-Ramirez, M. A., Bray, M., & Islam, T. (2012). Selection of classification techniques for land use/land cover change investigation. *Advances in Space Research*, 50(9), 1250–1265. doi:10.1016/j.asr.2012.06.032.
- [48] Dhingra, S., & Kumar, D. (2019). A review of remotely sensed satellite image classification. *International Journal of Electrical and Computer Engineering (IJECE)*, 9(3), 1720. doi:10.11591/ijece.v9i3.pp1720-1731.
- [49] Li, H., Dou, X., Tao, C., Wu, Z., Chen, J., Peng, J., Deng, M., & Zhao, L. (2020). RSI-CB: A large-scale remote sensing image classification benchmark using crowdsourced data. *Sensors (Switzerland)*, 20(6). doi:10.3390/s20061594.
- [50] Deng, C., & Wu, C. (2013). The use of single-date MODIS imagery for estimating large-scale urban impervious surface fraction with spectral mixture analysis and machine learning techniques. *ISPRS Journal of Photogrammetry and Remote Sensing*, 86, 100–110. doi:10.1016/j.isprsjprs.2013.09.010.
- [51] Rwanga, S. S., & Ndambuki, J. M. (2017). Accuracy Assessment of Land Use/Land Cover Classification Using Remote Sensing and GIS. *International Journal of Geosciences*, 08(04), 611–622. doi:10.4236/ijg.2017.84033.
- [52] Nappo, N., Peduto, D., Mavrouli, O., van Westen, C. J., & Gullà, G. (2019). Slow-moving landslides interacting with the road network: Analysis of damage using ancillary data, in situ surveys and multi-source monitoring data. *Engineering Geology*, 260. doi:10.1016/j.enggeo.2019.105244.
- [53] Butt, A., Shabbir, R., Ahmad, S. S., & Aziz, N. (2015). Land use change mapping and analysis using Remote Sensing and GIS: A case study of Simly watershed, Islamabad, Pakistan. *Egyptian Journal of Remote Sensing and Space Science*, 18(2), 251–259. doi:10.1016/j.ejrs.2015.07.003.